Cerium-loaded algae exoskeletons for active corrosion protection of coated AA2024-T3

Denissen, Paul J.; Garcia, Santiago J.

DOI
10.1016/j.corsci.2017.09.019

Publication date
2017

Document Version
Final published version

Published in
Corrosion Science: the journal on environmental degradation of materials and its control

Corrosion Science 128 (2017) 164–175

Contents lists available at ScienceDirect

Corrosion Science

journal homepage: www.elsevier.com/locate/corsci

Cerium-loaded algae exoskeletons for active corrosion protection of coated AA2024-T3

Paul J. Denissen, Santiago J. Garcia*

Delft University of Technology, Faculty of Aerospace Engineering, Kluyverweg 1, 2629 HS Delft, The Netherlands

ARTICLE INFO

Keywords:
Diatomaceous Earth
Microcarrier
Biosilica
Corrosion Inhibitor
Inhibition
Raman
EIS
Anticorrosion
AA2024
Cerium
Coating

ABSTRACT

The use of micron sized nanoporous diatom algae exoskeletons for inhibitor storage and sustained corrosion protection of coated aluminium structures upon damage is presented. In this concept the algae exoskeleton allows local inhibitor loading, limits the interaction between the cerium and the epoxy/amine coating and allows for diffusion-controlled release of the inhibitor when needed. The inhibitor release and corrosion protection by loaded exoskeletons was evaluated by UV/Vis spectrometry, a home-built optical-electrochemical setup, and Raman spectroscopy. Although this concept has been proven for a cerium-epoxy-aluminium alloy system the main underlying principle can be extrapolated to other inhibitor-coating-metal systems.

1. Introduction

Two of the major challenges faced by scientists replacing toxic and carcinogenic hexavalent chromium (CrVI) −based corrosion inhibitors by environmentally friendly ones are (i) the reduction of the negative inhibitor-coating matrix interactions that limit the new inhibitors efficiency, and (ii) the control over the release of the inhibitor in time [1]. For this reason several encapsulation methods have been proposed in the last decade. The most common and successful concepts use 2 dimensional (2D) inorganic nanoparticles (e.g. montmorillonites [2], bentonites [3] and hydrotalcites [4]) and since more recently 3 dimensional (3D) inorganic nanocarriers (e.g. zeolites [5,6] and halloysites [7]). Such carriers allow controlling the inhibitor release by different mechanisms (e.g. diffusion, pH, redox, ion exchange) while at the same time prevent unwanted inhibitor reactions with the surrounding polymer matrix and too fast inhibitor release leading to blistering [1]. Despite the significant progress and reported evidence for nanocarriers yielding protection of small damages (< 100 μm width scratches) for short periods of immersion time, their long-term protection of relatively large damages is constantly under question. This, together with their limited versatility, often synthesis complexity and insufficient local release capacity motivates the constant search for alternatives. In this work we introduce the use of diatom algae exoskeletons as carriers for corrosion inhibitors allowing lower inhibitor-matrix interactions, high local inhibitor storage and time-based release leading to sustained protection at damaged coated metals under immersion in salt solution.

Diatoms are a major group of unicellular algae with the unique feature of forming highly ordered hollow nanoporous silica exoskeletons (named frustules). Each of the estimated 100.000 extant species as well as the species found as mineral (diatomaceous earth) has a distinctive frustule (typically two symmetric sides hold together) which varies in size (from 2 μm to 4 mm), shape (star, cylinder, disk, oval, etc) and nanopore distribution and size [8]. For their characteristics the diatom exoskeletons are described as forming “pill-box” structures [9]. The availability, morphological characteristics and potential application of the bio-based diatom exoskeletons as carriers has recently attracted significant attention in the biomedical field where their use as drug delivery systems in fluid media has been studied [10–18]. Nevertheless, to the best of our knowledge, no dedicated studies of such silica based structures for corrosion inhibition have been reported in the scientific literature.

The proof of concept is here demonstrated for an epoxy-amine coating on an aerospace aluminium alloy AA2024-T3 system. Cerium nitrate was used as the model corrosion inhibitor for two reasons: (i) trivalent cerium (Ce^{3+}) ions are known for being excellent corrosion inhibitors in copper-rich aluminium alloys as AA2024-T3, and (ii) the industrial application of cerium containing inhibitors is highly limited by its reactivity with the surrounding coating matrix [19,20]. Cerium

* Corresponding author.
E-mail addresses: p.j.denissen@tudelft.nl (P.J. Denissen), s.j.garciaespallargas@tudelft.nl (S.J. Garcia).

http://dx.doi.org/10.1016/j.corsci.2017.09.019
Received 28 February 2017; Received in revised form 14 September 2017; Accepted 15 September 2017
Available online 19 September 2017
0010-938X/

nitrate was here stored into refined diatomaceous earth (DE) and its loading, release kinetics and corrosion inhibition efficiency of bare A-A2024-T3 in salt solution studied by real-time UV/VIS spectroscopy, scanning electron microscopy (SEM), energy-dispersive X-ray spectroscopy (EDS) and Raman spectroscopy. The active corrosion protection of the cerium-loaded DE particles (Ce-DE) was then evaluated in a particle-loaded epoxy coating by a home-made in-situ optical-electrochemical setup after creating highly controlled scratches of 130 µm width at the bottom of the scratch. The results obtained are compared to those obtained for an unloaded epoxy coating and two epoxy coatings directly loaded with cerium nitrate and potassium dichromate respectively. Although potassium dichromate is not typically used in coating systems due to its high solubility leading to blistering, the very fast action and high efficiency to protect large damages after short immersion times makes it a very useful model inhibitor to compare to and was therefore used in this study. The in-situ optical-electrochemical approach allowed obtaining real-time optical and electrochemical information on the corrosion/protection processes. This approach decreased the subjectivity and difficulty of interpreting traditional electrochemical signals of damaged corrosion inhibiting coatings. The analysis of the results showed a significant delay of the on-set and kinetics of the degradation process when the Ce-DE were used compared to the protection achieved by the direct addition of cerium nitrate to the coating. The role of the cerium ions on the corrosion inhibition was further confirmed by a post-test analysis of the damaged site by SEM-EDS and Raman spectroscopy. While the protection offered by the inhibiting species was detected with both techniques, the higher spatial resolution of the Raman signal at the scratch gained additional information on the interaction between cerium species and copper-rich intermetallic phases. The results here presented prove the high potential of the use of diatom exoskeletons to encapsulate corrosion inhibitors to avoid coating-inhibitor negative interactions and improve active corrosion protection in coated systems.

2. Experimental

2.1. Materials and preparation

Diatomaceous earth Diafil 525 mainly consisting of cylinder shaped diatom exoskeletons was supplied by Profiltra Customized Solutions (The Netherlands, NL). The as-received diatomaceous earth consists of 89.0 wt.% amorphous silica (SiO_2), a tapped powder bulk density of 0.42 g/cm^3 and a mean particle size of 12 µm. Cerium nitrate hexahydrate ($Ce(NO_3)_3$ $6H_2O$) and Potassium dichromate ($K_2Cr_2O_7$) with > 99% purity were purchased from Sigma-Aldrich. Commercial 2 mm thick bare AA2024-T3 sheet obtained from Kaizer Aluminium was used as metallic substrate. Commercially available bisphenol-A based epoxy resin (Epikote™ 828) and amine crosslinker (Ancamine®2500) were supplied by AkzoNobel (NL) and used as received to form the coating binder [21]. Xylene with a purity of 99% was used as epoxy solvent. All aqueous solutions for the particle doping, corrosion and release studies were prepared using Milipore® Elix 3 UV filtered water.

2.2. Refined diatomaceous earth (DE)

In order maximize the amount of intact diatom exoskeletons and reduce the impurities content (i.e. non-silica) a refining process was applied based on the work of Zhang et al. [22]. Fig. 1 shows the schematic illustration of the refining process whereby 8.0 g of as-received diatomaceous earth was suspended in 120 ml demineralized water and sonicated for 30 min. This was left in unstirred condition for 30 min to allow the silica intact exoskeletons to settle down. The supernatant (containing the impurities and small diatom parts) was discarded with the help of a glass pipette. This settling process was repeated 5 times (without sonication). Finally the settled particles were filtered using a Whatman® grade 595 paper filter and dried in a vacuum oven at 60 °C for 24 h. The refined diatomaceous earth, named DE for simplicity across the manuscript, was used in the rest of the study as the corrosion inhibitor carrier.

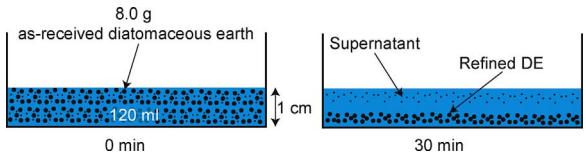

Fig. 1. Schematic illustration of the refining process of the diatomaceous earth.

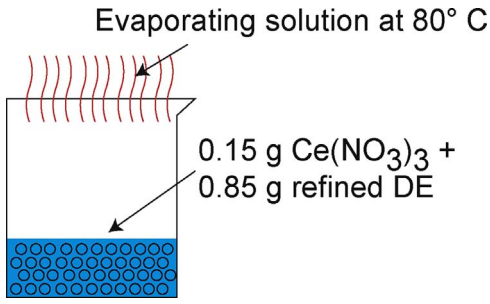

Fig. 2. Schematic illustration of the DE doping process leading to Ce-DE particles.

2.3. DE doping with cerium nitrate

For the doping procedure as illustrated in Fig. 2, a powder mixture of 0.85 g refined DE and 0.15 g cerium nitrate hexahydrate was added to 2.0 ml demineralized water. The mixture was then placed on a shaking table at 320 rpm for 24 h followed by complete drying in an oven at 80 °C under ambient atmosphere for another 24 h. As a result of the process a DE powder containing 15 wt.% of cerium nitrate was obtained. The loaded powder was then screened through a stainless steel sieve of 50 µm aperture to reduce agglomerates and conform the here on called cerium-doped DE (Ce-DE).

2.4. Coatings preparation

The AA2024-T3 metal sheets were cut into pieces of 25 × 50 mm prior to surface modification and coating application. The metal surface preparation followed previously reported procedures [6] consisting of the following sequential steps: (i) removal of native oxide layer and surface chemistry homogenization using SiC sandpapers down to grit 320; (ii) surface roughness formation by Scotch Brite 3 M “Clean N Finish grade AVFN”; (iii) degreasing with acetone; and (iv) immersion in a 2 M sodium hydroxide (NaOH) aqueous solution for 10 s followed by rinsing with distilled water and air drying in order to increase the surface hydroxide (OH) fraction and therefore adhesion with the subsequent organic coating.

The organic coatings were prepared using a mixture of Epikote™ 828, Ancamine®2500 and Xylene (2.70:1.57:1 wt ratio) as reported elsewhere [21]. Five coating systems (named Epoxy, DE, Ce, Ce-DE and Cr) were formulated as summarized in Table 1. In all cases the epoxy-amine-xylene mixture was first high-shear mixed for 5 min at 2500 rpm in a high-speed mixer. In order to reduce possible side reactions with the epoxy/amine matrix the mixtures were then let pre-cure at ambient conditions for 30 min before the corrosion inhibiting components (cerium nitrate powder, DE, Ce-DE or potassium dichromate) were added. The mixtures were then manually stirred to form a homogeneous mixture, applied on the AA2024-T3 coupons by a 100 µm spiral bar coater and cured at 60 °C for 24 h as reported elsewhere to achieve complete crosslinking [6]. After curing the coated panels were stored in a desiccator until 30 min before testing. The final pigment volume concentration (PVC) in the dry coatings was calculated using

Table 1
Overview of the coatings compositions, sample coding and relevant coating parameters.

Sample Coding (epoxy-amine based coating)	Particle content (wt. %)[a]	Thickness (μm)	PVC (%)	Active inhibitor content (moles/kg binder)
Epoxy	0[b]	110 ± 20	0	0
DE	12[c]	80 ± 20	25	0
Ce	2[d]	80 ± 20	0.5	0.04
Ce-DE	14[e]	110 ± 20	25	0.04
Cr	2[f]	100 ± 20	0.8	0.06

[a] Minhibiting particles/M epoxy-amine coating; where M is mass.
[b] coating Epoxy contains no particles (epoxy-amine clear-coat).
[c] coating DE contains 12 wt.% refined diatomaceous earth (DE) particles.
[d] coating Ce contains 2 wt.% cerium nitrate hexahydrate ($Ce(NO_3)_3\ 6H_2O$).
[e] coating Ce-DE contains 14 wt.% refined diatomaceous earth (DE) doped with cerium nitrate hexahydrate ($Ce(NO_3)_3\ 6H_2O$).
[f] coating Cr contains 2 wt.% potassium dichromate ($K_2Cr_2O_7$).

equation 1.

$$PVC\,(\%) = \frac{V_{inhibitor} + V_{DE}}{V_{inhibitor} + V_{DE} + V_{epoxy/amine}} * 100\% \quad (1)$$

Where $V_{inhibitor}$ is the volume of cerium nitrate powder, V_{DE} is the volume of refined DE, and $V_{epoxy/amine}$ is the volume of the epoxy-amine binder in the system. It should be noted that the amount of active species in weight was kept constant as shown in Table 1, resulting in a lower molar content of cerium compared to the molar content of chromium calculated as shown in Section 1 of the support information (S.I.).

2.5. Scratch damage in coated metals for corrosion inhibition evaluation

Reproducible and controlled 5 mm long and 130 μm wide scratches (at the bottom of the scratch) were created on the coated panels with a CSM Microscratch tester using a 100 μm Rockwell C diamond tip in multi-pass mode. For this, the tip was programmed to give 5 passes at each load of 5N, 10N and 15N at the same location until the AA2024-T3 substrate was reached.

2.6. Testing methods and equipment

2.6.1. Diatomaceous earth particle analysis

A JEOL SJM-840 scanning electron microscope coupled with energy dispersive X-ray spectroscopy (SEM-EDS) was used to analyse the topological and elemental composition of the diatomaceous earth powders. Images were recorded at 5 kV accelerating voltage. Samples were coated with a 15 nm gold layer before SEM examination.

A Malvern Mastersizer 2000 particle size distribution analyser (PSD) was used to evaluate the effect of the refining process of the as-received diatomaceous earth. The effect of the cerium doping on the crystalline structure of the exoskeletons was monitored with a Bruker D8 advanced X-ray diffractometer (XRD) using Cu-Kα radiation (λ = 1.54 Å) with scattering angles (2θ) of 5 − 130°.

2.6.2. Real-time inhibitor release from DE carrier

Cerium inhibitor release was studied in real immersion time with a PerkinElmer LAMBDA 35 UV/VIS spectrometer. For the real-time release studies the UV/VIS cuvette was modified as shown in the S.I. (Fig. S1) allowing for measurements without the need of aliquot extraction. Samples containing $Ce(NO_3)_3$ salt and Ce-doped DE were placed inside a cone-shaped Whatman® grade 1 paper filter on top of the cuvette filled with demineralized water. UV–vis spectra were taken every second. In order to ensure an even inhibitor dispersion in the cuvette and to avoid false measurements the solution was constantly magnetically stirred at 1400 rpm. Both samples were analysed in threefold. Cerium inhibitor release was followed by the variation in the 252 nm wavelength signal corresponding to Ce III as shown in the S.I. (Fig. S2) and reported in literature [23,24]. For the inhibitor concentration quantification from the UV signal a linear calibration curve was constructed with an R^2 of 0.999 over 10 predefined inhibitor concentrations in the range 10^{-3} M to 10^{-5} M, as shown in the S.I (Fig. S3). The UV/VIS calibration curve was validated with a PerkinElmer Optima 3000DV inductively coupled plasma analyser (ICP). An acceptable margin of error on the final cerium concentration of around 10% was measured probably due to small weighting variations and hygroscopic effect of the cerium nitrate.

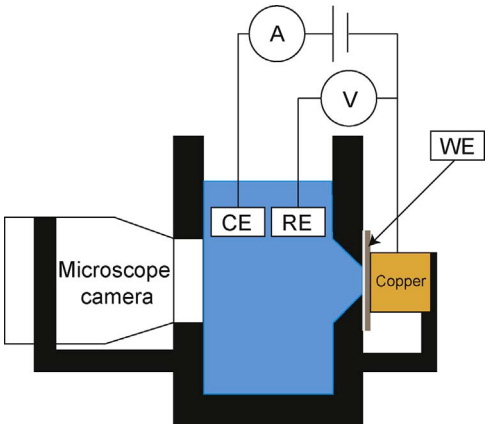

Fig. 3. Schematic illustration of the optical-electrochemical set-up used in the study. The microscope camera is visible on the left hand of the image and the analysed sample (working electrode) on the right hand.

2.6.3. In-situ optical-electrochemical set-up (corrosion protection studies)

The corrosion protection behaviour of the scratched coatings was monitored with a home-built in-situ optical-electrochemical set-up during immersion in 0.05 M sodium chloride (NaCl) aqueous solution. A minimum of two repeats per coating system was performed. The set-up consisted of a three-electrode electrochemical cell coupled to a microscope camera allowing for real-time electrochemical and surface optical analysis at the damaged site. A schematic illustration of the set-up is shown in Fig. 3 and a photo of the set up for more clarity can be found the S.I. (Fig. S4). A potentiostat Metrohm PGSTAT 302 and a universal serial bus (USB) Celestron handheld digital microscope camera with 1.2 megapixel (Mpx) resolution were used for the electrochemical tests and optical monitoring respectively. The coated sample was placed vertically in the electrochemical cell by clamping it with a copper block to a hole made on one side of the electrochemical cell as reported elsewhere [25]. Opposite to the studied sample, a hole closed with a transparent Plexiglas window allowed aligning the handheld digital microscope to the exposed sample thereby optically monitoring the immersed sample. Both the camera and the three-electrode electrochemical cell were placed inside a Faraday cage to avoid external interferences. During immersion Electrochemical Impedance Spectroscopy (EIS) and Open Circuit Potential (OCP) measurements were performed. The three-electrode electrochemical cell consisted of a silver/silver-chloride (Ag/AgCl) reference electrode (RE), 6.6 mm diameter graphite rod as counter electrode (CE) and the coated and damaged AA2024-T3 samples as working electrode (WE). The frequency range of study was 10^5-10^{-2} Hz, with applied amplitude of 10 mV root mean square (RMS) over OCP to minimize the influence of the test on the metal-coating system while still obtaining a reliable response. The potentiostat was controlled with a USB interface through the software package NOVA V1.11.1.

The microscope camera and the potentiostat were programmed to take an optical image and an EIS measurement every hour so that the optical images correspond to the moment of the EIS analysis. It should be here noted that all the relevant surface variations were found within a 0.9 mm lateral distance from the centre of the scratch as well as from

scratch ends as shown in the S.I. (Fig. S5). The absence of optical variations outside that area confirmed the good barrier properties of the coatings during the studied immersion time. The optical images were then converted to 8-bit greyscale files and processed with the use of ImageJ free software as shown in the S.I. (Figs. S6-S10). Once the images were converted to 8-bit, the lighter background corresponding to the undamaged area was removed using a bimodal threshold method. The increase of the dark area over time with reference to the initial dark areas is caused by the degradation of the system ($\Delta A_{degraded}$) and can be can calculated using equation 2:

$$\Delta A_{degraded}(\%) = \frac{A_t - A_0}{A_s} * 100\% \quad (2)$$

Where A_t is the increased dark area (degraded area) at time t, A_0 the initial dark area (e.g. caused by scratch) and A_s the total studied area of 12 mm^2.

2.6.4. Cerium interaction with the exposed AA2024-T3 metal surface

In order to confirm the involvement of cerium in the active corrosion protection at damage sites both SEM-EDS and Raman spectroscopy analysis were performed at the bottom of the scribe (i.e. metal surface) of the damaged coated samples used in the optical-electrochemical study. For the Raman analysis a Renishaw inVia reflex microscope equipped with a research-grade Leica microscope objective at 50× magnification and numerical aperture of 0.55 was used. A 532-nm laser light with an effective laser power of 32 mW in 1 s excitation measurements was employed. Control tests were performed on a copper block, cerium oxide precipitates, and on bare AA2024-T3 exposed to inhibited and non-inhibiting solutions, which are included in the support information.

3. Results and discussion

3.1. Particle characterization

Fig. 4 shows a set of SEM images and EDS spectra of the diatom exoskeletons before (4a and 4c) and after (4b and 4c) the refining process. Fig. 4d shows the effect of the refining process on the particle size distribution. From the SEM images it becomes clear that the refining process significantly reduced the amount of broken diatoms and other impurities of the as received diatomaceous earth as intended. The SEM inserts in Figs. 4a and 4b further confirm the removal of very small particles blocking the nano-pores in the as-received exoskeletons. The particle size analysis showed a near Gaussian-shaped size distribution with an increased peak centred at 12 µm (Fig. 4d) as well as a drop of the small fraction particles after the refining process. A detailed SEM image analysis of the refined diatomaceous earth (DE) allowed recognising exoskeletons of four clearly different diatom species whereby the, by far, most abundant one was identified as *sp. Aulacoseira* with exoskeletons similar to those reported in literature having a cylindrical pill-box structure with nanopores of around 500 nm evenly distributed around the exoskeleton wall [11].

EDS analysis (Fig. 4c) was used to determine the effect of the refining process on the removal of the chemical species other than the silica of the diatom shell. Fig. 4c shows the predominance of silicon (Si) and oxygen (O) constituents as expected for diatom silica (SiO_2) exoskeletons. Small traces of aluminium (Al), Iron (Fe), Calcium (Ca) and Magnesium (Mg) were also detected and assigned to impurity oxides (Al_2O_3, Fe_2O_3, $CaCO_3$, CaO, and MgO) as reported in previous studies [12]. The presence of the same constituent elements in the refined diatomaceous earth as in the as received ones revealed that the refining process used was not capable of removing, at least not fully, the oxide impurities. The presence of the impurities in the clean DE did nevertheless not have an effect on the ulterior cerium doping when the doping procedure proposed in this work was employed. This was proven by a further study on the chemical treatments of the DE with alkali and acidic solutions leading to the disappearance of the impurity oxides but no significant difference in the Ce-uptake as shown in the S.I (Figs. S11 and S12 ; section 4). As the impurities did not have a significant effect in the doping it was decided to skip the acid and alkali post-treatments to simplify the process.

Diatom exoskeleton loading with corrosion inhibitors was

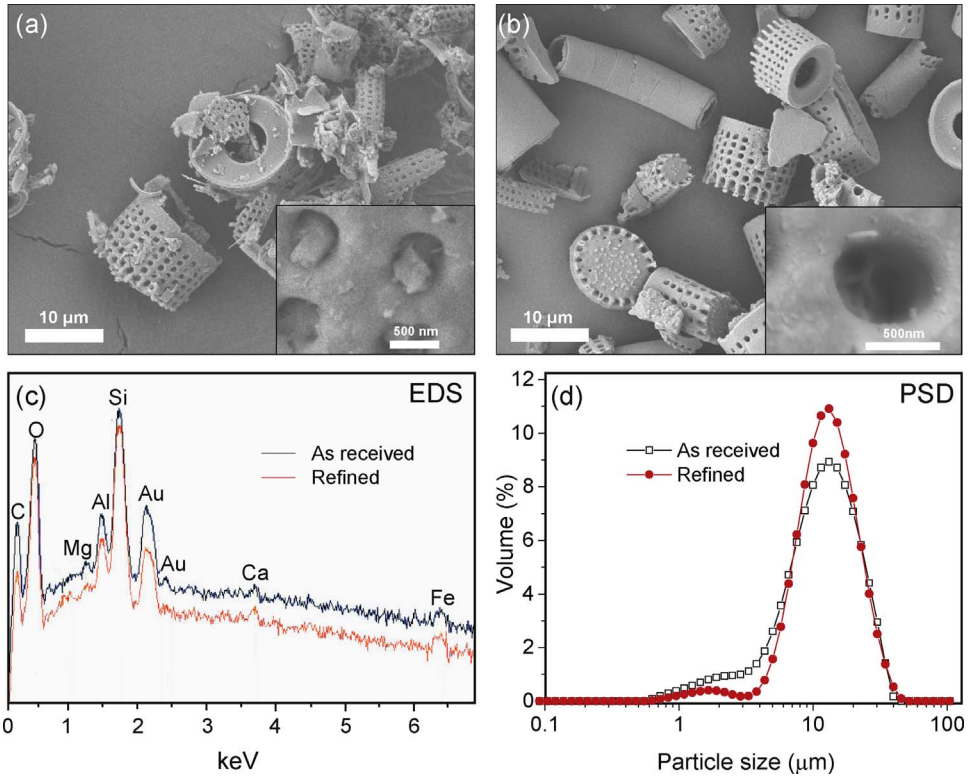

Fig. 4. SEM images of diatom exoskeletons and their open porous structure (insets) for as-received (a) and refined (b) diatomaceous earth. Energy dispersive spectroscopy (EDS) spectrum and particle size distribution of the two samples are shown in (c) and (d) respectively.

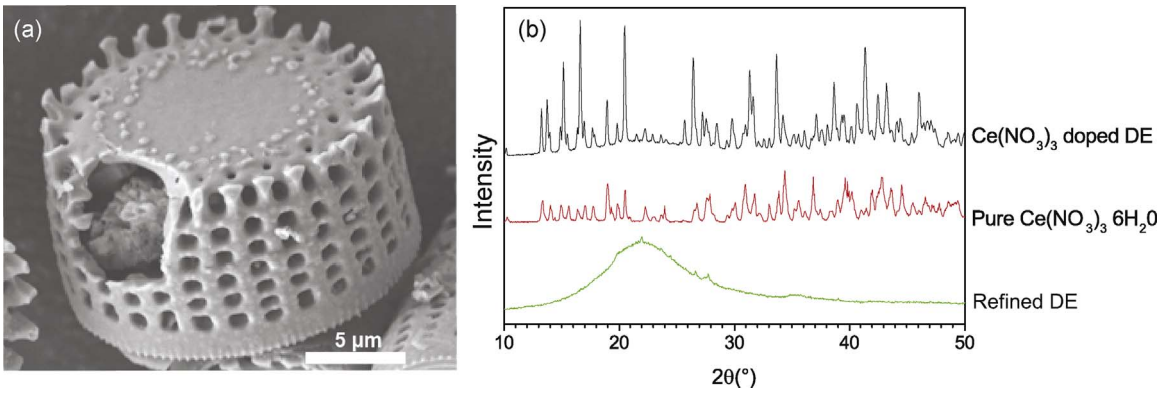

Fig. 5. (a) SEM image of a single fractured diatom exoskeleton after corrosion inhibitor. (b) Comparative XRD spectra of refined DE, $Ce(NO_3)_3$ $6H_2O$ corrosion inhibitor salt, and Ce-DE.

confirmed by SEM and XRD analysis (Fig. 5). The XRD spectra in Fig. 5b show that the DE (refined diatomaceous earth) primarily consisted of amorphous silica with some minor diffraction peaks at 22.0° and 26.6° corresponding to crystalline structures of quartz and cristobalite. The XRD spectra for the Ce-DE (cerium doped DE) shows the amorphous silica baseline combined with crystalline peaks corresponding to Ce $(NO_3)_3$. The increased intensity of the peaks compared to pure Ce $(NO_3)_3$ $6H_2O$ is presumably caused by the decrease of water in the crystal lattice due to drying and localized deposition on the diatom silica surface. The results confirm that, during the doping process, the cerium inhibitor did not change its crystalline structure and remained as an inorganic salt primarily inside the diatom exoskeletons body space and nanopores, thereby confirming the success of the developed doping procedure.

Fig. 6 shows the difference in the release behaviour (dissolution and diffusion) of the $Ce(NO_3)_3$ salt directly placed in the paper filter of the UV–vis system as shown in the S.I. (Fig. S1) and that of the cerium salt contained in the Ce-DE particles. By analysing the release plots it can be seen that the inhibitor is fully dissolved after one hour in both cases, which is in line with the diffusion coefficients of the ionic species in aqueous media [26]. The release response for both systems is comparable whereby the release at the beginning increases exponentially due to the high solubility of $Ce(NO_3)_3$ and ends asymptotically due to the equal distribution of $Ce(NO_3)_3$ in the UV/VIS cuvette. Interestingly, the release curve for the Ce-DE particles is slower than that of the cerium salt over the entire time domain. Such a delay can be attributed

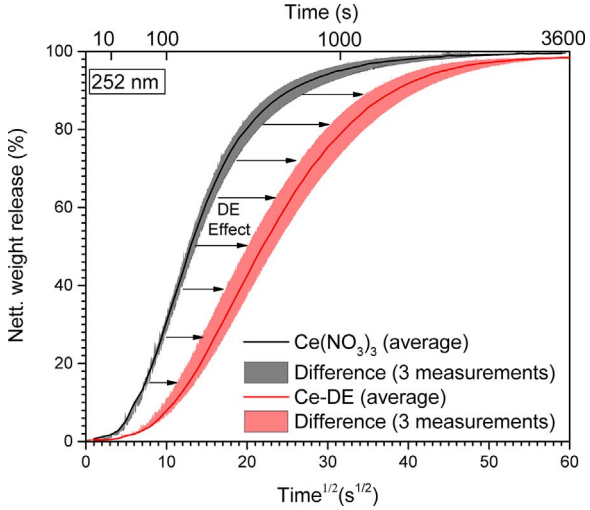

Fig. 6. Cerium release kinetics of cerium nitrate from the salt powder (black) and from cerium-loaded DE particles (Ce-DE) (red) obtained with a real-time UV/VIS spectroscopy from the 252 nm wavelength. (For interpretation of the references to colour in this figure legend, the reader is referred to the web version of this article.)

to the chemical or topological trapping of the cerium included in the DE exoskeleton structure together with the delay due to diffusion through the porous walls of the diatom exoskeletons. Furthermore, the increasing separation in time between the two release curves plotted against $t^{1/2}$ shows the entire release spectrum of Ce from DE is delayed between 10 and 10^3 seconds with respect to the cerium salt in the filter. These results confirmed that the cerium inhibitor loaded in the DE structure was able to come out by a time diffusion controlled process in aqueous solution as intended.

The active corrosion protection by the release of cerium from the Ce-DE particles in solution was studied by a detailed SEM/EDS and Raman study on bare AA2024-T3 immersed in 0.05 M NaCl solutions (S.I.; section 5 Fig. S13 and section 6 Figs. S14-S17 respectively). Despite the delay with respect to the salt observed with UV-VIs, the results confirmed that the cerium is released from the DE particles at a sufficient rate to prevent local corrosion by the formation of protective cerium precipitates at copper-rich phases.

3.2. Inhibitor-loaded particle/epoxy coating interaction

The presence of cerium inhibitor in the coating matrix and a validation of its active state when Ce-DE particles were used was monitored by SEM and colour changes (yellowing). Fig. 7 shows the SEM-EDS micrograph of a fractured epoxy coating containing Ce-DE particles. The fractured plane shows a DE cylindrical particle (from the top) embedded in the epoxy matrix. The EDS analysis further confirmed the presence of high cerium concentrations inside the exoskeleton with a low carbon signal of the polymeric matrix. This confirms that the cerium inhibitor remained in the inner volume of the DE during the particle mixing with the epoxy coating and is therefore available for local release as intended.

When the coatings were prepared a fast deep yellowing was observed in the case of the Ce coating (Cerium nitrate salt directly added to the epoxy-amine coating). This yellowing can be seen in the S.I. (Section 7; Fig. S18) when the amine was added directly to the cerium nitrate salt after one hour (Fig. S18a, b). Such yellowing has been well reported and indirectly attributed to the oxidation of Ce III to Ce IV by the amines [27–30]. Although this reaction does not lead to any significant changes in the overall mechanical properties of the epoxy-amine matrix it has been reported as one of the factors leading to lower inhibition efficiencies than expected in Ce-rich epoxy coatings [29]. A reduction in the yellowing is therefore desired as it indicates a lower matrix-inhibitor reaction and therefore an increase of the expected inhibition power in the Ce-loaded coating systems. When the amine was added to the Ce-DE particles (Fig. S18c and S18d) a significant decrease in the yellowing was observed during the 1 h test. Such a result is in agreement with the intended isolation of the Cerium inhibitor from the epoxy-amine matrix by means of the silica diatom exoskeleton thereby leaving higher amounts of Ce III available in the interior of the particles

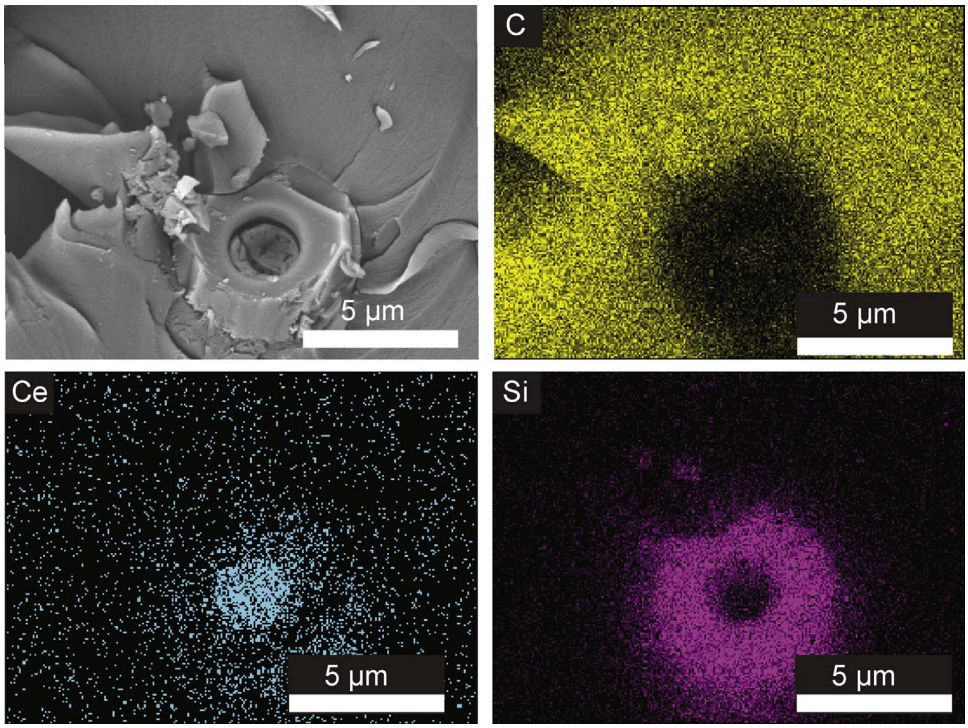

Fig. 7. SEM and EDS micrographs for C, Ce and Si of the fractured plane of an epoxy coating loaded with Ce-DE. The SEM/EDS analysis confirms the presence of high Ce-concentrations in the diatom frustule after mixing with the epoxy-amine coating.

ready to act as corrosion inhibitors.

3.3. Corrosion protection of damaged coatings

Fig. 8 shows selected EIS Bode plots (|Z| and phase) for the scratched coatings after 3 h (8a and 8c) and 90 h (8b and 8d) immersion. At 3 h immersion it becomes clear that the Cr coating shows the highest total impedance (|Z|) and phase shift of all coatings, particularly in the low frequency range. Such high impedance in the Cr coating indicates a fast active corrosion protection due to the inhibitor high solubility and its high inhibiting power. On the other hand, the observed instabilities for the other coatings at short immersion times highlight the high activity at the scribe. After 90 h of immersion all coating systems are more stable and differences amongst them become more clear. Three coatings showed a total impedance increase from 3 h to 90 h: Cr, CE (2) and Ce-DE (2). Although the increase over time is often used to confirm sufficiently protecting systems [31] it remains unlikely to be the case for Ce (2) due to its lower initial and final total impedance value compared to the non-inhibiting Epoxy reference coating. On the other hand, the Cr and the two Ce-DE coatings show higher total impedance values than the Epoxy, DE and Ce coatings. Such higher impedance and the absence of clear signs in the phase related to pit formation seem to suggest an active corrosion protection in the case of the Cr and Ce-DE systems. Due to the complexity of the degradation processes at and around the scribes impedance analysis are generally complemented with other post-test studies. Yet this allows only to identify the final degradation state and not to undoubtfully relate impedance observations with degradation processes. To gain more information of the on-going degradation in time the optical images during the electrochemical measurements were analysed with the optical-electrochemical setup described in the experimental section and the support information.

Fig. 9 shows selected optical microscopy images of the scratched coatings after 3 h and 90 h of immersion taken during the electrochemical measurements. The formation of delaminated areas, corrosion products (grey “clouds”) and local corrosion sites (dark spots) can clearly be seen at the scribe of the non-inhibited coatings (Epoxy and DE). Similar features can be observed in the case of the Ce coatings (cerium salt added to the coating matrix) although up to a minor extent. These optical observations point at the low or non-corrosion protection offered by the Epoxy, DE and Ce coatings. On the other hand, both Ce-DE coatings and the Chromium containing coating (Cr) do not show significant variations with the immersion time at the scribe, which remains bright in both cases, thereby indicating a clear active corrosion protection of the damaged site. For the two Ce-DE coatings a dark area under the coating appeared next to the scratch (indicated with the red oval in Fig. 9). Interestingly, the two dark areas appeared at a similar location, are of about the same size, and they both grew slowly in size and colour intensity after their first appearance until stabilization. Although the degradation phenomenon that caused this process is not yet clear it seems clear that the process was somehow controlled by the inhibitors in the coating. The presence of these degradation areas could justify the relatively low impedance values of the Ce-DE coatings compared to the epoxy, DE and Ce coatings despite the clear bright scribes indicating no corrosion.

A dedicated image analysis of the images taken with the in-situ optical-electrochemical setup followed the EIS study. In the analysis the degraded area at and around the scratch with immersion time was calculated and represented by the parameter $\Delta A_{degraded}$. This parameter is obtained after a sequential image analysis of the micrographs by converting the images into grey scale, removing the lighter background and calculating the increase of the degraded area in time as explained in the experimental section and the support information. In this work the ‘degraded area’ is identified as darkening and is related to corrosion signs such as oxide formation, localized corrosion (e.g. pits) and delamination. When plotting the $\Delta A_{degraded}$ parameter in% against the immersion time both the on-set time of the optically-detectable ‘degradation processes’ and the kinetics of the degradation process itself (slope after the on-set time) can be obtained. A more detailed description of the quantification process can be found in the S.I. (section 3). Fig. 10 shows the degraded area around the scratch for the two DE, Ce and Ce-DE coatings. The two non-inhibiting DE coatings show a stable period with no visible degradation during the first 30 h followed by a fast propagation of the degraded area at similar kinetics of 0.13 and 0.20% per hour. On the other hand in the Ce coatings first signs of degradation start short after immersion but grow at a much lower pace of 0.08 and 0.07% per hour, thereby highlighting the moderate

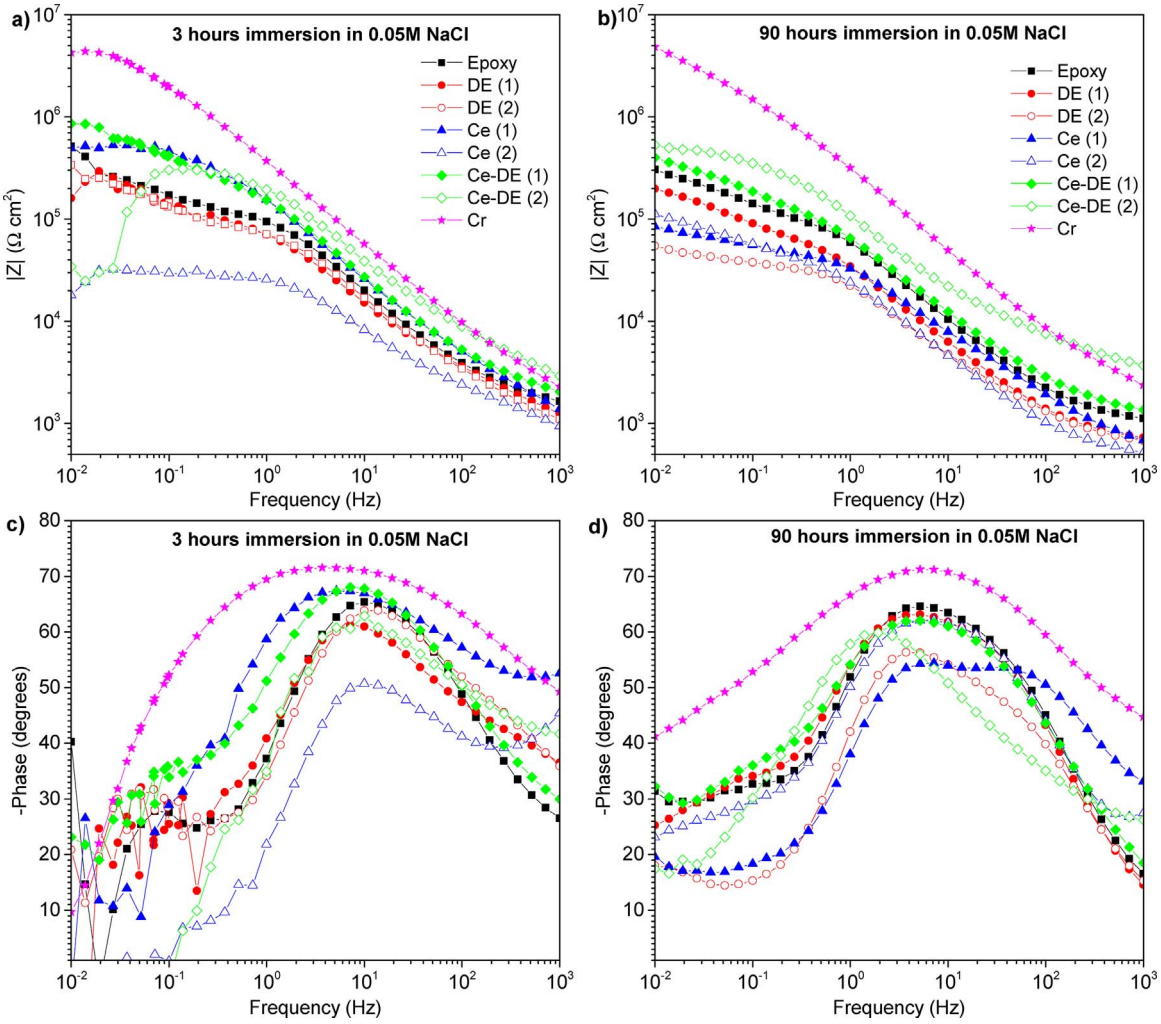

Fig. 8. Bode plots showing the total impedance (a and b) and phase (c and d) EIS plots for the coatings (1x Epoxy, 2x DE, 2x Ce, 2x Ce-DE and 1x Cr) after 3h (a and b) and 90 h (c and d) immersion in 0.05 M NaCl.

corrosion inhibiting effect of Ce. Based on the detail image analysis, the initial stable period seen in the DE coatings was attributed to a higher adhesion strength between the coating and the metal substrate compared to the Ce coatings. Such interphase improvement leads to a delay of the delamination on-set but not to a decrease in the delamination growth kinetics as there is no inhibiting effect, A different result was found for the Ce-DE inhibited samples. In this case, the samples remain stable with no visible degradation during the first 70 h, at which some degradation is detected around the scribe (red oval in Fig. 9) and propagate at a degradation growth kinetics of around 0.002% per hour.

In order to facilitate the reading of the impedance results in relation to degradation and protection Fig. 11 was developed. In Fig. 11 the variation of the total impedance at a given frequency (0.01 Hz) between two consecutive time measurements (i.e. Z_t/Z_{t-1}) and the OCP are plot against immersion time. The normalizing of the impedance to the previous measurement was used to filter out possible effects of initial coating properties, delamination, and changes in barrier protection. Impedance at 0.01 Hz and OCP time evolution were chosen for the comparison between samples as this frequency highlights the on-going processes at the metal surface related to corrosion or protection phenomena [32] and the OCP also relates to delaminations and other underfilm corrosion processes [33,34]. Results for the variation in impedance obtained at other frequencies (e.g. 0.014 and 0.1 Hz) did not lead to trend or interpretation changes but show less enhanced signals as shown in the S.I. (Fig. S24).

Fig. 11a and 11b show the impedance variation and OCP evolution over time for the two non-inhibited coatings DE (1) and DE (2), respectively. Both systems show instabilities and high impedance jumps during the first 27 h of immersion. Such a behaviour is in good agreement with initial local corrosion such as pitting, dealloying and replating processes typical observed on non-inhibited AA2024-T3 [20]. After 30 h the impedance for both systems stabilize and the OCP dropped from −0.5 V until it reached a plateau at −0.7 V for coating DE (1) and −0.75 V for DE (2). This drop is in agreement with values reported in literature for dealloyed AA2024-T3 [20] and is in agreement with the onset of delamination and underfilm corrosion optically observed and plot in Fig. 10. Fig. 11c and 11d show the impedance variation and OCP evolution over time for the Ce containing coatings, Ce (1) and Ce (2), respectively. Ce (1) shows impedance instabilities until 60 h with two very strong impedance jump events at 10 and 27 h. These two impedance jumps are accompanied by a sudden drop in OCP followed by a slow recovery back to −0.5 V during the consecutive hours. This recovery can be related to the passivation of the metallic surface by cerium species (i.e. inhibiting event) as is not observed in non-inhibited samples. At 60 h (two times longer than the non-inhibited system) the impedance stabilizes and the OCP drops, indicating that the dealloying has been reduced but not stopped and that delaminations take place as can also be seen by the change in degradation kinetics shown in Fig. 10 after 60 h. On the other hand, coating Ce (2) only shows one single instability after 3 h coupled to a sudden OCP drop down to −0.77 V, indicating a fast degradation and no (significant) inhibition effect of the contained cerium. This trend is also in good

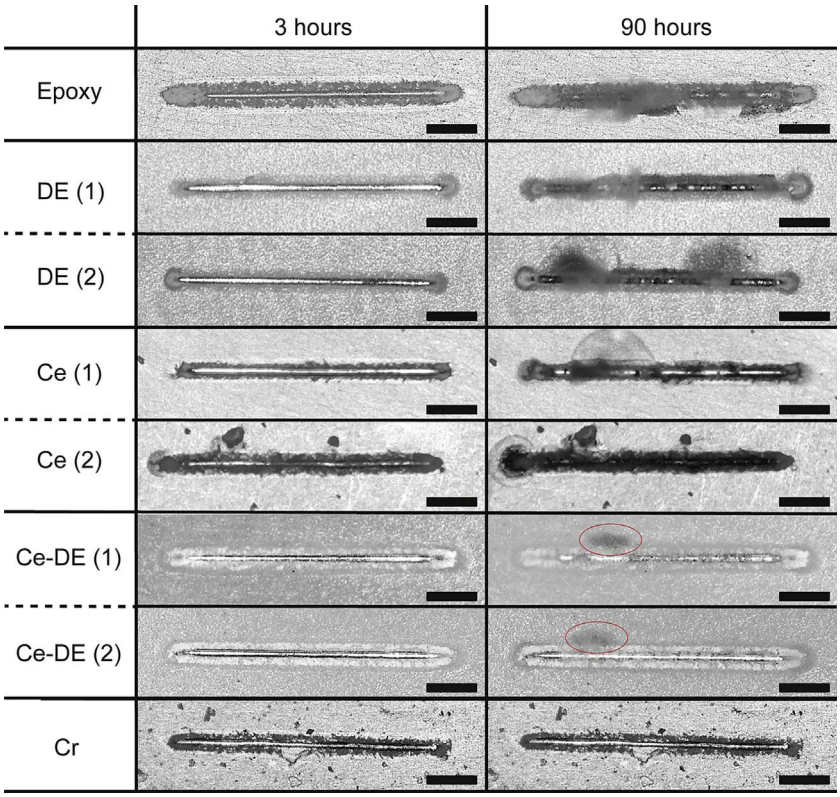

Fig. 9. Optical microscopy images obtained with the optical-electrochemical setup for the coatings (1x Epoxy, 2x DE, 2x Ce, 2x Ce-DE and 1x Cr) after 3 and 90 h immersion in 0.05 M NaCl. The red oval in the Ce-DE marks the formation and development of a dark area under the Ce-DE coating. (For interpretation of the references to colour in this figure legend, the reader is referred to the web version of this article.)

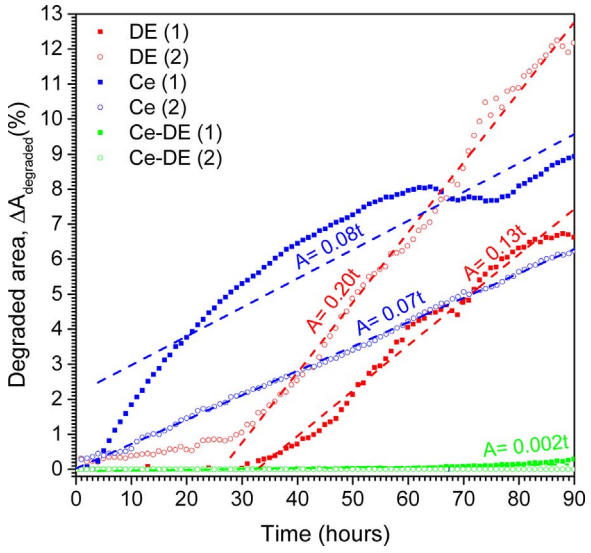

Fig. 10. Optical variation of the degraded area ($\Delta A_{degraded}$) including regressions after the on-set time obtained from the processed optical images for coating systems CE, DE and Ce-DE during immersion in 0.05 M NaCl.

agreement with the high amount of corrosion attack visible in Fig. 9 and the stable degradation kinetics in Fig. 10 directly after immersion. The big differences between the two Ce coating systems clearly show that adding $(Ce(NO_3)_3$ salt pigments directly to the epoxy binder results in uncontrolled behaviour with high scatter in the level of corrosion protection achieved probably due to differences in inhibitor dispersion degree as well as reactivity of the cerium with the epoxy matrix as indicated by the strong yellowing of the coating. Fig. 11e and f show the impedance variation and OCP evolution over time for the coatings containing cerium doped DE particles, Ce-DE (1) and Ce-DE (2) respectively. In both cases the OCP remains between −0.5 V and −0.6 V over the whole exposure time. Sudden drops in OCP are again coupled to impedance instabilities which are slowly recovered with the immersion time. These trends are in agreement with the slow degradation growth kinetics of 0.002% area increase per hour (Fig. 10) as well as the absence of features related to abundant oxide formation (grey clouds) and local corrosion sites (dark spots) at the scribe observed in the other samples (Fig. 9). When compared to the Ce-coating, the behaviour of the Ce-DE coating suggests that the new encapsulation concept allowed, as intended, for a fast and sufficient local cerium release during the first immersion hours followed by a sustained inhibitor supply capable of maintaining the overall corrosion protection level for the studied time. Yet the presence of lateral delaminations shown in Fig. 9 and the undoubtful better results with the chromated system highlight the room for improvement of this new concept despite the initial promising results.

In order to identify any direct relationship between the observed inhibition at the scribe and the inhibitor release a detailed optical, SEM-EDS and Raman spectroscopy analysis was performed at the scribe at the end of the immersion time. Fig. 12 shows the optical and SEM micrographs of the DE, Ce and Ce-DE damaged coatings after 4 days of immersion. It can clearly be seen that the corrosion products completely block the exposed aluminium surface at the scratch in the case of the DE and, to a minor extent, the Ce coating. On the other hand, the metal surface remains clearly visible and partially shiny in the case of the Ce-DE (1) coating. Despite the clear lack of oxide products and measured protection in the Ce-DE coating, trenching could be observed (red oval in Fig. 12) and assigned to localized corrosion attack around intermetallic sites as reported elsewhere for non-inhibited AA2024-T3 during the first hours of immersion [35]. In the same sample, signs of oxide cracking as observed in AA2024-T3 directly exposed to Cerium ions was also observed. The low presence of features possibly related to aluminium oxides and subsurface attack [37] confirms the local action of the released cerium ions from the coating and its interaction with the intermetallic compounds (IMs). The presence of cerium at the scribe was confirmed by SEM-EDS analysis (Fig. 13). In this image it can be seen how the diatom exoskeletons remain in the coating (Si signal)

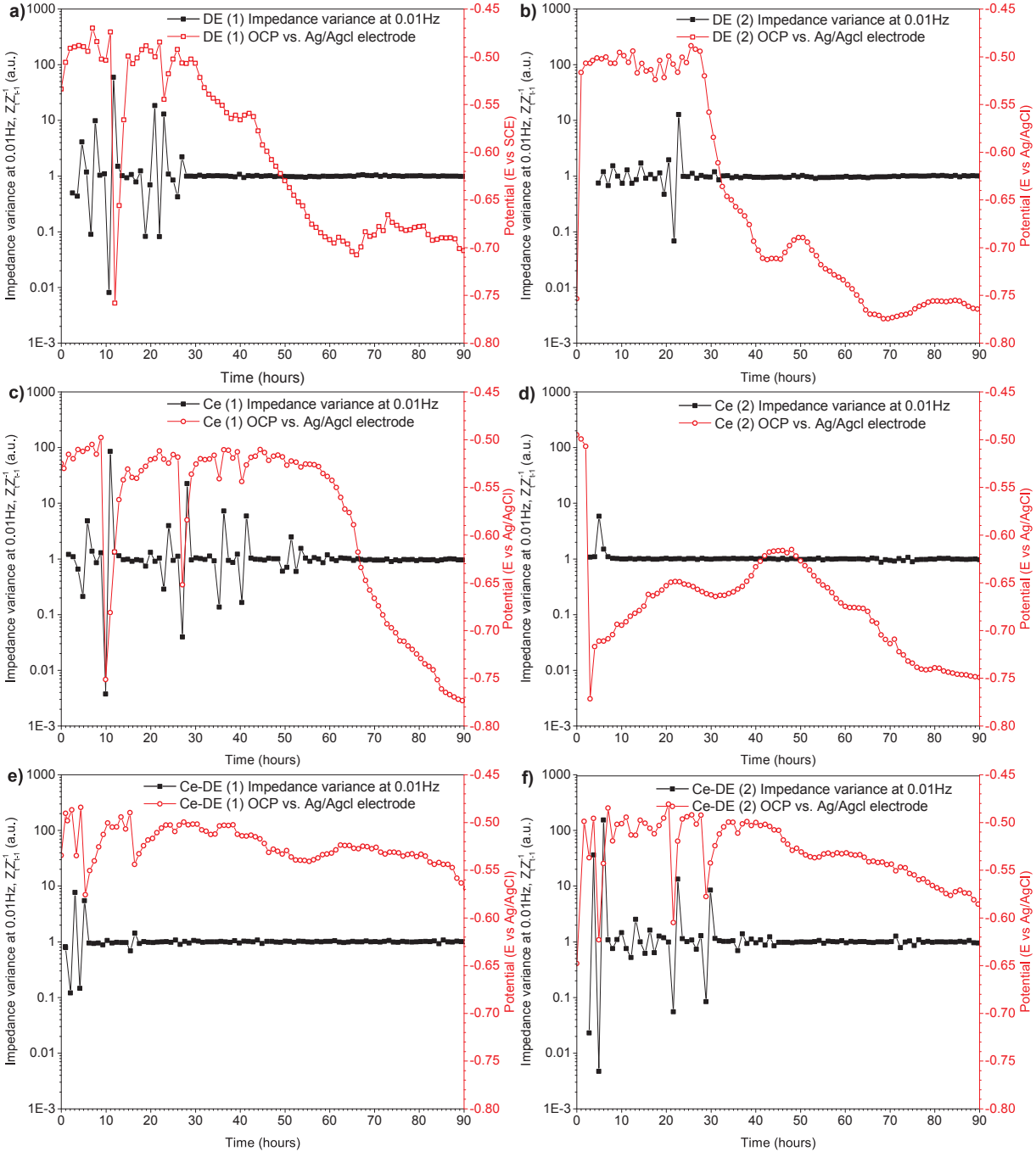

Fig. 11. Open Circuit potential (OCP) and the impedance variance Z_t/Z_{t-1} at 0.01 Hz evolving over time for (a) DE (1), (b) DE (2), (c) Ce (1), (d) Ce (2), (e) Ce-DE (1), and (f) Ce-DE (2).

while the cerium is located primarily at the scribe (metal surface) confirming the cerium was released from the coating. It should be noted that similar cerium signals were detected in the case of the Ce-coating. However, EDS is highly sensitive to Ce but quantification is not possible. It is therefore assumed that even if some cerium was released from the Ce-coating, the amount was not sufficient or was released too slowly to lead to any significant corrosion protection of the damaged site.

As SEM-EDS was not capable of identifying the exact location of cerium ions the scribe was further analysed by Raman spectroscopy. For the purpose, detailed analysis was performed on some control samples; a copper block and cerium oxide precipitates on a glass substrate to establish the wavelengths of the characteristic peaks related to cerium oxides and copper sites (S.I.; section 6, Fig. S14, S15). Two main characteristic sharp peaks were then detected: (i) a 625 cm^{-1} peak assigned to Cu_2O; and (ii) a peak at the F_{2g} Raman active mode at 463 cm^{-1} attributed to the symmetrical stretching of the Ce-8O vibrational units as reported elsewhere [36–40] and confirmed by the presence of CeO_2 precipitates on glass. Subsequently the interaction of cerium ions with the AA2024-T3 substrate was studied for Ce-DE particles and $Ce(NO_3)_3$ in solution (S.I.; section 6, Figs. S16 and S17). It was then observed that the cerium peak signal was always detected at the same locations where the copper oxide peak signal was found being thus possible to determine the location of Cu-rich IMs and Cerium deposition. Finally a Raman analysis of the scribe of the Ce-DE coated sample was performed. Fig. 14 shows the Raman shift region of interest. Again the two characteristic peaks were found at the same locations on the metallic surface although the Raman shift corresponding to the

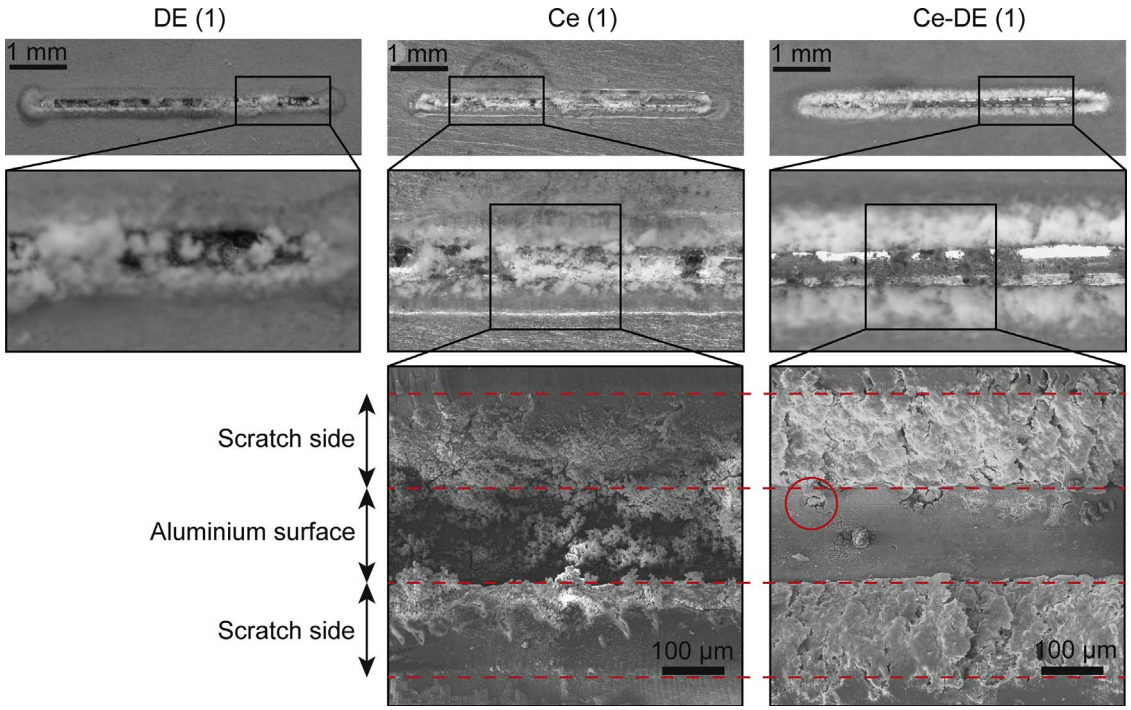

Fig. 12. Optical microscopy and SEM low secondary electron image (LEI) at the damaged sites of the DE (1), Ce (1) and Ce-DE (1) coatings after 4 days immersion in 0.05 M NaCl. The red circle indicates trenching around IM particles at the scribe of the Ce-DE (1) coating system. (For interpretation of the references to colour in this figure legend, the reader is referred to the web version of this article.)

CeO_2 was found to be broader than that of the CeO_2 precipitates (Fig. S15; SI) and having a maximum peak located at Raman shifts ranging from 455 to 461 cm^{-1} depending on the location. Such a variation can be explained by the disorder of the oxygen sublattice, changes in the valence band, or grain-size induced effects [36,39]. The Raman analysis at the scribe clearly shows the interaction of the Ce ions at Cu-rich sites thereby confirming that the observed inhibiting effect of the Ce-DE coatings with the optical-electrochemical setup can be related to sufficient release of cerium at the damage site followed by its interaction preferentially at cathodic Cu-rich sites. The use of the different optical-electrochemical techniques and local analysis of inhibitor-metal interaction at the scribe site with Raman spectroscopy confirmed the appropriateness of using diatom exoskeletons to encapsulate efficient inhibitors that otherwise cannot be used due to their tendency to react with the surrounding matrix. Such an approach opens the path for the development of more efficient Cr-free technologies based on inhibitor release from organic coatings.

4. Conclusions

The potential use of bio based algae exoskeleton as powerful carriers for local inhibitor storage leading to high active protection at damaged sites in coated metals is presented. The concept, based on the use of diatom algae silica exoskeletons, has been proven for the protection of

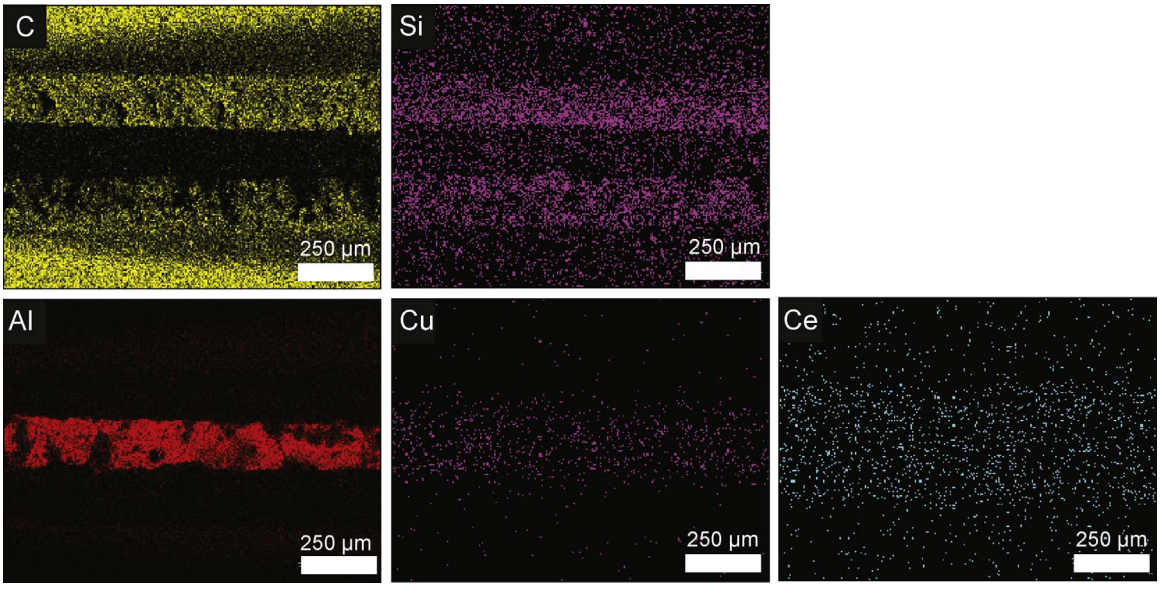

Fig. 13. EDS elemental mapping for the Ce-DE (1) coating showing: the location of the organic coating (C map), the diatom exoskeletons (Si map), the metallic substrate (Cu, Al maps) and the cerium (Ce map).

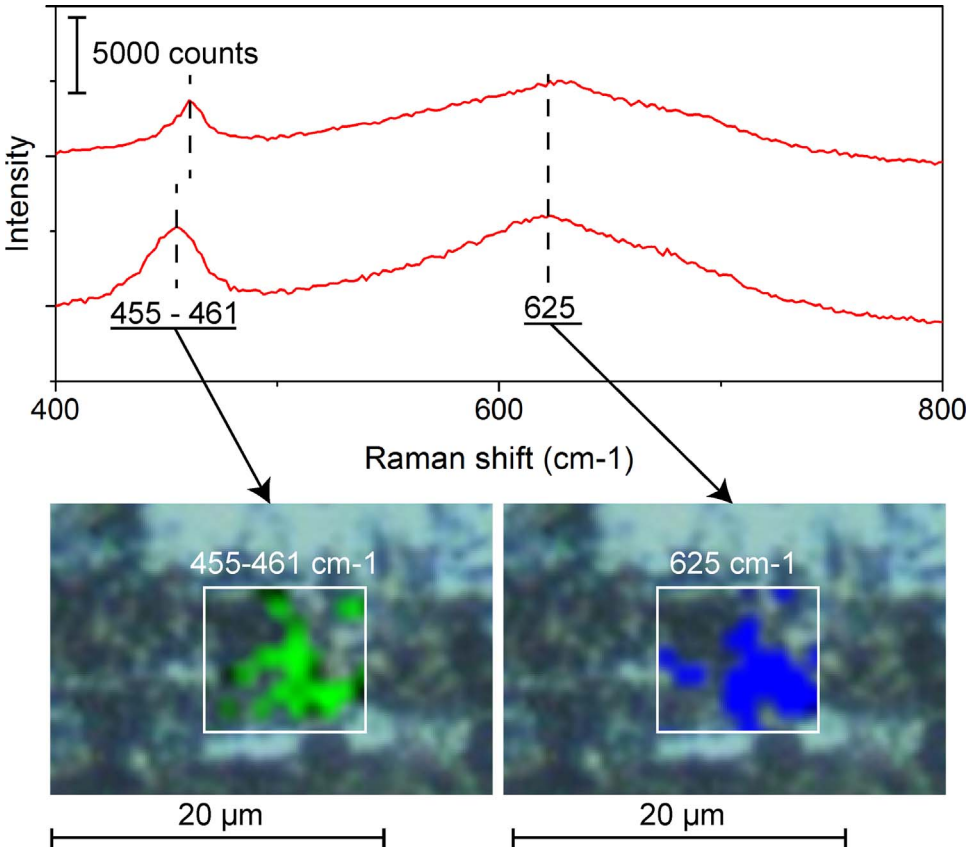

Fig. 14. Raman spectrum for Ce-DE (1) at the damaged sites of the coatings after 4 days of immersion and the Raman shift intensity plots at 455–461 cm-1 and 625 cm-1. Image clearly shows the preferential deposition of Ce (455–461 cm^{-1}) at Cu-rich sites (625 cm^{-1}) for two random locations.

AA2024-T3 structures by cerium nitrate corrosion inhibitor. In order to evaluate the corrosion protection at damaged sites a home-made optical-electrochemical set-up was used. High levels of active corrosion protection at damage sites were obtained for at least 4 immersion days; this being about 4 more times than coatings using the same inhibitor without the diatom shell. The high protection levels achieved are due to the isolation of the cerium inhibitor by the silica algae cage from the epoxy coating reducing unwanted reactions, the elevated inhibitor storage in the silica cages and the fast and sustained release of the cerium inhibitor at the damaged site. The study also shows the feasibility of developing protective systems based on fast release and inhibition at damaged sites followed by a time-sustained or on-demand release of corrosion inhibitors supplied at a sufficient concentration to ensure the long term protection. Despite the obvious corrosion inhibition offered by the newly developed Ce doped diatomaceous earth particles a faster and sufficient inhibitor release during the first immersion hours would be beneficial to prevent the formation of all kind of localized corrosion signs (e.g. trenching) and ensure long-time protection. The use of inhibitor loaded algae exoskeleton particles for sustained corrosion inhibition here presented is not restricted to cerium and epoxy coatings on aluminium substrates but should be regarded as a generic concept with high versatility and potential for developing environmentally friendly active corrosion protection in coated metals.

Acknowledgments

The authors would like to acknowledge Prof. Sybrand van der Zwaag for his sustained support and the helpful and detailed discussions. The authors also acknowledge the Faculty of Aerospace Engineering at the Delft University of Technology for the financial support.

Appendix A. Supplementary data

Supplementary data associated with this article can be found, in the online version, at http://dx.doi.org/10.1016/j.corsci.2017.09.019.

References

[1] H.R. Fischer, S.J. Garcia, A.E. Hughes, J.M.C. Mol, M.L. Zheludkevich, R.G. Buchheit (Eds.), Act. Prot. Coatings New-Generation Coatings Met. Springer, Netherlands Dordrecht, 2016, pp. 139–156.
[2] M.G. Hosseini, M. Jafari, R. Najjar, Surf. Coatings Technol. 206 (2011) 280–286.
[3] S. Bohm, H.N. McMurray, S.M. Powell, D.A. Worsley, Mater. Corros. 52 (2001) 896–903.
[4] R.G. Buchheit, S.B. Mamidipally, P. Schmutz, H. Guan, Corrosion 58 (2002) 3–14.
[5] R. Cai, Y. Yan, Corrosion 64 (2008) 271–278.
[6] E.L. Ferrer, A.P. Rollon, H.D. Mendoza, U. Lafont, S.J. Garcia, Microporous Mesoporous Mater. 188 (2014) 8–15.
[7] D. Fix, D.V. Andreeva, Y.M. Lvov, D.G. Shchukin, H. Möhwald, Adv. Funct. Mater. 19 (2009) 1720–1727.
[8] F.E. Round, R.M. Crawford, D.G. Mann, The Diatoms Biology & Morphology of the Genera, Cambridge University Press, 2007.
[9] Y. Wang, J. Cai, Y. Jiang, X. Jiang, D. Zhang, Appl. Microbiol. Biotechnol. 97 (2013) 453–460.
[10] M.S. Aw, M. Bariana, Y. Yu, J. Addai-Mensah, D. Losic, J. Biomater. Appl. 28 (2013) 163–174.
[11] M.S. Aw, S. Simovic, J. Addai-Mensah, D. Losic, Nanomedicine 6 (2011) 1159–1173.
[12] M.S. Aw, S. Simovic, Y. Yu, J. Addai-Mensah, D. Losic, Powder Technol. 223 (2012) 52–58.
[13] M. Bariana, M.S. Aw, D. Losic, Adv. Powder Technol. 24 (2013) 757–763.
[14] M. Milovic, S. Simovic, D. Losic, A. Dashevskiy, S. Ibric, Eur. J. Pharm. Sci. 63 (2014) 226–232.
[15] H. Zhang, M.A. Shahbazi, E.M. Makila, T.H. da Silva, R.L. Reis, J.J. Salonen, J.T. Hirvonen, H.A. Santos, Biomaterials 34 (2013) 9210–9219.
[16] P. Gnanamoorthy, S. Anandhan, V.A. Prabu, J. Porous Mater. 21 (2014) 789–796.
[17] I. Ruggiero, M. Terracciano, N.M. Martucci, L. De Stefano, N. Migliaccio, R. Tate, I. Rendina, P. Arcari, A. Lamberti, I. Rea, Nanoscale Res. Lett. 9 (2014) 329.
[18] T. Todd, Z. Zhen, W. Tang, H. Chen, G. Wang, Y.-J. Chuang, K. Deaton, Z. Pan, J. Xie, Nanoscale 6 (2014) 2073–2076.
[19] K.A. Yasakau, M.L. Zheludkevich, S.V. Lamaka, M.G.S. Ferreira, J. Phys. Chem. B 110 (2006) 5515–5528.
[20] S.J. Garcia, T.A. Markley, J.M.C. Mol, A.E. Hughes, Corros. Sci. 69 (2013) 346–358.

[21] M. Abdolah Zadeh, S. van der Zwaag, S.J. García, Surf. Coatings Technol. 303 (2016) 396–405.
[22] D. Zhang, Y. Wang, J. Pan, J. Cai, J. Mater. Sci. 45 (2010) 5736–5741.
[23] S. Joshi, E.A. Kulp, W.G. Fahrenholtz, M.J. O'Keefe, Corros. Sci. 60 (2012) 290–295.
[24] E.G. Heckert, A.S. Karakoti, S. Seal, W.T. Self, Biomaterials 29 (2008) 2705–2709.
[25] S.J. García, T.H. Muster, Ö. Özkanat, N. Sherman, A.E. Hughes, H. Terryn, J.H.W. de Wit, J.M.C. Mol, Electrochim. Acta 55 (2010) 2457–2465.
[26] F. Martelli, S. Abadie, J. Simonin, R. Vuilleumier, R. Spezia, Pure Appl. Chem. 85 (2013) 237–246.
[27] C. Wang, F. Jiang, F. Wang, Corros. Sci. 46 (2004) 75–89.
[28] L.S. Kasten, J.T. Grant, N. Grebasch, N. Voevodin, F.E. Arnold, M.S. Donley, Surf. Coatings Technol. 140 (2001) 11–15.
[29] J. Mardel, S.J. Garcia, P.A. Corrigan, T. Markley, A.E. Hughes, T.H. Muster, D. Lau, T.G. Harvey, A.M. Glenn, P.A. White, S.G. Hardin, C. Luo, X. Zhou, G.E. Thompson, J.M.C. Mol, Prog. Org. Coatings 70 (2011) 91–101.
[30] T. Seop Lim, H. Sam Ryu, S.-H. Hong, J. Electrochem. Soc. 160 (2012) C77–C82.
[31] P. Visser, M. Meeusen, Y. Gonzalez-garcia, H. Terryn, J. Electrochem. Soc. 164 (2017) 396–406.
[32] S.K. Poznyak, J. Tedim, L.M. Rodrigues, A.N. Salak, M.L. Zheludkevich, L.F. Dick, M.G. Ferreira, ACS Appl. Mater. Interfaces 1 (2009) 2353–2362.
[33] T.H. Muster, H. Sullivan, D. Lau, D.L.J. Alexander, N. Sherman, S.J. Garcia, T.G. Harvey, T.A. Markley, A.E. Hughes, P.A. Corrigan, A.M. Glenn, P.A. White, S.G. Hardin, J. Mardel, J.M.C. Mol, Electrochim. Acta 67 (2012) 95–103.
[34] F.J. Presuel-Moreno, H. Wang, M.A. Jakab, R.G. Kelly, J.R. Scully, J. Electrochem. Soc. 153 (2006) B486–B498.
[35] A. Boag, A.E. Hughes, A.M. Glenn, T.H. Muster, D. McCulloch, Corros. Sci. 53 (2011) 17–26.
[36] Z.D. Dohčević-Mitrović, M.J. Šćepanovića, M.U. Grujić-Brojčina, Z.V. Popovića, S.B. Boškovićb, B.M. Matovićb, M.V. Zinkevichc, F. Aldingerc, Solid State Commun. 137 (2006) 387–390.
[37] G.W. Graham, W.H. Weber, C.R. Peters, R. Usmen, J. Catal. 130 (1991) 310–313.
[38] W.H. Weber, K.C. Hass, J.R. McBride, Phys. Rev. B 48 (1993) 178–185.
[39] J. Twu, C.J. Chuang, K.I. Chang, C.H. Yang, K.H. Chen, Appl. Catal. B Environ. 12 (1997) 309–324.
[40] I. Kosacki, V. Petrovsky, H.U. Anderson, P. Colomban, J. Am. Ceram. Soc. 85 (2002) 2646–2650.